Methods for Measurement of Intermolecular NOEs by Multinuclear NMR Spectroscopy: Application to a Bacteriophage λ N-Peptide/*boxB* RNA Complex

Catherine Zwahlen,[‡] Pascale Legault,[‡] Sébastien J. F. Vincent,[‡] Jack Greenblatt,[§] Robert Konrat,[⊥] and Lewis E. Kay*[,‡]

Contribution from the Protein Engineering Network Centers of Excellence and Departments of Molecular and Medical Genetics, Biochemistry, and Chemistry, University of Toronto, Toronto, Ontario, Canada M5S 1A8, Banting and Best Department of Medical Research and Department of Molecular and Medical Genetics, University of Toronto, Toronto, Ontario, Canada M5G 1L6, and Institute of Organic Chemistry, University of Innsbruck, Innrain 52A, A-6060, Innsbruck, Austria

Received January 24, 1997. Revised Manuscript Received April 24, 1997[⊗]

Abstract: New pulse schemes for recording intermolecular NOEs in a molecular complex consisting of ^{15}N,^{13}C labeled and unlabeled components are presented. The pulse sequences select for magnetization transferred from protons on the unlabeled component to proximal protons of the labeled molecule. Filtering (suppression of signal from ^{13}C labeled molecules) is accomplished using adiabatic ^{13}C inversion pulses which are swept at a rate which is tuned according to the one-bond ^{1}H−^{13}C scalar coupling vs carbon chemical shift profile of the labeled molecule in the complex. Significantly improved spectra are obtained relative to data recorded with other purging schemes. Improvements are demonstrated in experiments where intermolecular NOEs between labeled RNA-unlabeled peptide and labeled protein−unlabeled peptide are recorded. A discussion of structural information obtained for a complex of the amino-terminal arginine rich domain of the N protein from bacteriophage λ and *boxB* RNA using the new methodology is presented.

Introduction

The development of multidimensional, multinuclear NMR spectroscopy has significantly impacted on the scope of problems that can be addressed using NMR methods.[1,2] For example, structures can now be obtained of proteins and protein complexes in the 20−30 kDa molecular weight range.[3,4] In the case of molecular complexes, a common approach involves uniform labeling of one of the components with ^{15}N and ^{13}C, while the second component remains unlabeled.[5,6] It is then possible to select for interactions (through-bond or through-space) connecting protons that either both are or are not one-bond scalar coupled to ^{15}N or ^{13}C spins and in this manner edit or filter spectra to obtain information about one of the components of the system. It is also possible to select for NOEs across the molecular interface by requiring that magnetization be transferred between a pair of protons, where only one of the protons is bound to a labeled heteroatom. The accuracy of the derived structure is particularly sensitive to both the number and fidelity of the intermolecular NOE assignments, and it is therefore important that sensitive and artifact-free methods be available for measuring such interactions.

Experiments for measuring intermolecular NOEs consist of a period in which proton magnetization originating from either ^{1}H−^{13}C or ^{1}H−^{15}N pairs is selected against (filtering) as well as an interval in which magnetization from protons which are one-bond coupled to either ^{15}N or ^{13}C spins is selected for (editing).[5,7,8] These periods are separated by an interval during which magnetization is transferred between proximal protons via the NOE. The process of selecting for ^{15}N- or ^{13}C-bound proton spins is extremely efficient for labeled molecules. However, schemes for purging proton magnetization from ^{1}H−^{13}C spin pairs, that is, selecting for protons that are not bound to ^{13}C carbons, are less efficient since one-bond ^{1}H−^{13}C scalar couplings can vary over a wide range (from approximately 120−220 Hz). Two different experimental strategies have been proposed for filtering. The first approach, pioneered by Wüthrich and co-workers,[7,9] makes use of a spin echo difference scheme, whereby ^{1}H−^{13}C or ^{1}H−^{15}N pairs are selected against on the basis of the difference in sign of magnetization originating from protons that either are or are not one-bond coupled to ^{13}C or ^{15}N spins. A second method, originally developed by Ernst and colleagues, employs a series of heteronuclear purge pulses and delays to create a low pass filter, where proton magnetization is allowed to pass only if the ^{1}H−X scalar coupling is smaller than some threshold.[10] Thus, magnetization from ^{1}H−^{13}C or ^{1}H−^{15}N spin pairs is effectively suppressed.

In the past several years a large number of pulse schemes have been reported for measuring intermolecular correlations that are variants of the methods proposed by the groups of

[‡] Protein Engineering Network Centers of Excellence and Departments of Molecular and Medical Genetics, Biochemistry, and Chemistry.

[§] Banting and Best Department of Medical Research and Department of Molecular and Medical Genetics.

[⊥] University of Innsbruck.

[⊗] Abstract published in *Advance ACS Abstracts,* July 1, 1997.

(1) Bax, A.; Grzesiek, S. *Acc. Chem. Res.* **1993**, *26*, 131.
(2) Clore, G. M.; Gronenborn, A. M. *Science* **1991**, *252*, 1309.
(3) Ikura, M.; Clore, G. M.; Gronenborn, A. M.; Zhu, G.; Klee, C. B.; Bax, A. *Science* **1992**, *256*, 632.
(4) Zhang, H.; Zhao, D.; Revington, M.; Lee, W.; Jia, X.; Arrowsmith, C. H.; Jardetzky, O. *J. Mol. Biol.* **1994**, *229*, 735.
(5) Ikura, M.; Bax, A. *J. Am. Chem. Soc.* **1992**, *114*, 2433.
(6) Folkers, P. J. M.; Nilges, M.; Folmer, R. H. A.; Konings, R. N. H.; Hilbers, C. W. *J. Mol. Biol.* **1994**, *236*, 229.
(7) Otting, G.; Senn, H.; Wagner, G.; Wüthrich, K. *J. Magn. Reson.* **1986**, *70*, 500.
(8) Otting, G.; Wüthrich, K. *J. Magn. Reson.* **1989**, *85*, 586.
(9) Otting, G.; Wüthrich, K. *J. Magn. Reson.* **1988**, *76*, 569.
(10) Kogler, H.; Sorensen, O. W.; Bodenhausen, G.; Ernst, R. R. *J. Magn. Reson.* **1983**, *55*, 157.

S0002-7863(97)00224-2 CCC: $14.00

Wüthrich and Ernst.[5,11−15] Applications of the methods to protein−ligand,[5,16] protein−DNA,[4,17] and protein−RNA[18] systems have been described. However, all of the methods suffer to some extent from artifacts which derive from the difficulty in selecting exclusively for protons that are not coupled to ^{13}C nuclei. Here we present a new approach for purging $^{1}H-^{13}C$ spin pairs based on the use of frequency swept carbon inversion pulses. As described below, the sweep rate of such pulses can be tuned to offer significantly improved suppression levels relative to the existing class of experiments. Results from experiments performed on a complex of the $^{15}N,^{13}C$ labeled dNumb PTB domain[19] (160 residues) with unlabeled ligand (10 residues) and the unlabeled amino-terminal 22 residues of the bacteriophage λ N protein (N^{1-22}) in 1:1 complex with $^{15}N,^{13}C$ labeled *boxB* RNA[20] (19 nucleotides) are presented illustrating the utility of the new method. Finally, a brief discussion of the preliminary structural information obtained on the basis of the intermolecular NOEs observed for the N^{1-22}/*boxB* RNA complex is included.

Materials and Methods

Both unlabeled and $^{15}N,^{13}C$ labeled *boxB* RNA (sequence given in Figure 1a) were enzymatically synthesized by *in vitro* transcription with T7 RNA polymerase and synthetic single-stranded DNA templates using either unlabeled or ^{15}N, ^{13}C labeled NTPs.[21,22] Unlabeled and $^{15}N,^{13}C$ labeled N^{1-22} peptides, comprising the amino-terminal 22 residues of the N protein from bacteriophage λ, were synthesized as GST-fusion constructs cloned from pGex-2T (Pharmacia) and expressed in TOPP2 cells (Stratagen). The amino terminal two residues of the N^{1-22} peptide (lower case in the sequence below) derive from the cleavage site and are not part of the wild-type N protein sequence. Hence numbering for N^{1-22} begins at methionine (sequence = g s M D A Q T R R R E R R A E K Q A Q W K A A N) which is the first residue of the wild-type protein. Details of sample production will be given elsewhere. NMR samples were prepared by titrating concentrated *boxB* RNA (~30 mM) dissolved in NMR buffer into a sample of the N^{1-22} peptide. After the titration to a 1:1 complex, the sample buffer for the complex was exchanged with the NMR buffer consisting of 25 mM succinate-d_4 (Aldrich), 100 mM NaCl, 0.2 mM EDTA, 0.05 mM NaN_3, pH 5.5 in a Centricon-3 concentrator. For samples dissolved in D_2O lyophilization was performed several times with resuspension in 99.996% D_2O (Aldrich). Final sample concentrations were approximately 3 mM. Samples of the $^{15}N,^{13}C$ labeled N-terminal SH3 domain from drk (drkN SH3) and the $^{15}N,^{13}C$ labeled C-terminal SH2 domain from phospholipase $C_{\gamma 1}$ (PLCC) in complex with a 12-residue unlabeled phosphotyrosine-containing-peptide (pY1021) comprising the high affinity binding site on the platelet-derived growth factor receptor were prepared as described by Zhang and Forman-Kay[23] and Pascal *et al.*,[16] respectively. Finally, a sample of the $^{15}N,^{13}C$ labeled dNumb PTB domain in complex with the 10 residue peptide, AYIGPYLGGK, was prepared as described previously.[19] Sample conditions were as follows: drkN SH3, 1.0 mM, 50 mM sodium phosphate, pH 6.0, 90% H_2O/10% D_2O, 2 M guanidine hydrochloride; PLCC SH2, 1.5 mM, 100 mM sodium phosphate, >99% D_2O, pD 6.3 (uncorrected); dNumb PTB, 1.4 mM, 20 mM sodium phosphate, 150 mM NaCl, 0.1 mM benzamidine, 0.1 mM EDTA, 20 mM deuterated DTT, >99% D_2O, pD 6.0 (uncorrected).

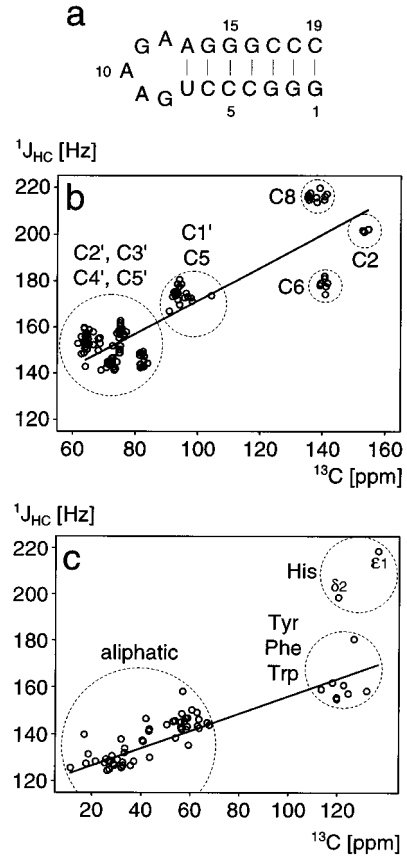

Figure 1. (a) Sequence and proposed secondary structure of *nut*L *boxB* RNA from bacteriophage λ. Two additional G−C base pairs (G1−C19 and G2−C18) were added to the wild-type hairpin stem. (b and c): Correlation between $^{1}J_{HC}$ (Hz) and ^{13}C chemical shift (ppm) in ribonucleic acids and proteins. (b) The RNA database covers almost all proton−carbon bonds from $^{15}N,^{13}C$ labeled *boxB* RNA in 1:1 complex with unlabeled N^{1-22}. Linear regression analysis gives the following equation (solid line): $^{1}J_{HC} = (0.710 \pm 0.037$ Hz/ppm$)\,\delta_C + 101.0 \pm 3.5$ Hz. A similar equation [$^{1}J_{HC} = (0.716$ Hz/ppm$)\,\delta_C + 100.4$ Hz] was obtained using the data from Varani *et al.*[29] (c) $^{1}J_{HC}$ vs carbon chemical shift for proteins. The database consists of residues in N^{1-22} in complex with *boxB* RNA. A number of amino acids are not represented in N^{1-22}; data from the missing residues has been supplemented with $^{1}J_{HC}$ values measured from the PLCC SH2[16] and the drkN SH3[23] domains. This protein database (used to calculate the relation between $^{1}J_{HC}$ and δ_C) has been constructed to simulate a standardized hundred-residue protein where the percentage of each residue corresponds to its average natural abundance in proteins[28] (see Materials and Methods). Linear regression analysis gives the following equation (solid line): $^{1}J_{HC} = (0.365 \pm 0.010$ Hz/ppm$)\,\delta_C + 120.0 \pm 0.5$ Hz.

One bond $^{13}C-^{1}H$ scalar coupling values, $^{1}J_{HC}$, were compiled from $^{13}C-^{1}H$ correlation spectra and a 3D HCCH-TOCSY spectrum[24,25] (PLCC SH2 only) each recorded without ^{13}C decoupling in the acquisition dimension. Constant-time $^{13}C-^{1}H$ correlation experiments[26,27] were recorded for the measurement of aliphatic and sugar $^{1}J_{HC}$ couplings. Couplings for the aromatics were obtained using

(11) Folkers, P. J. M.; Rolmer, R. H. A.; Konings, R. N. H.; Hilbers, C. W. *J. Am. Chem. Soc.* **1993**, *115*, 3798.
(12) Lee, W.; Revington, M.; Arrowsmith, C. H.; Kay, L. E. *FEBS Lett.* **1994**, *350*, 87.
(13) Fesik, S. W.; Luly, J. R.; Erickson, J. W.; Zapatero-Abad, C. *Biochemistry* **1988**, *27*, 8297.
(14) Gemmecker, G.; Olejniczak, E. T.; Fesik, S. W. *J. Magn. Reson.* **1992**, *96*, 199.
(15) Ogura, K.; Terasawa, H.; Inagaki, F. *J. Biomol. NMR* **1996**, *8*, 492.
(16) Pascal, S. M.; Singer, A. U.; Gish, G.; Yamazaki, T.; Shoelson, S. E.; Pawson, T.; Kay, L. E.; Forman-Kay, J. D. *Cell* **1994**, *77*, 461.
(17) Omichinski, J. G.; Clore, G. M.; Schaad, O.; Felsenfeld, G.; Trainor, C.; Appella, E.; Stahl, S. J.; Gronenborn, A. M. *Science* **1993**, *261*, 438.
(18) Battiste, J. L.; Mao, H.; Rao, N. S.; Tan, R.; Muhandiram, D. R.; Kay, L. E.; Frankel, A. D.; Williamson, J. R. *Science* **1996**, *273*, 1547.
(19) Li, S.-C.; Lai, V. K.-M.; Gish, G. D.; Parris, W. E.; Geer, P.; Forman-Kay, J. D.; Pawson, T. *J. Biol. Chem.* **1996**, *271*, 31855.
(20) Tan, R.; Frankel, A. D. *Proc. Natl. Acad. Sci. U.S.A.* **1995**, *92*, 5282.
(21) Milligan, J. F.; Groebe, D. R.; Witherell, G. W.; Uhlenbeck, O. C. *Nucleic Acids Res.* **1987**, *15*, 8783.
(22) Nikonowicz, E. P.; Sirr, A.; Legault, P.; Jucker, F. M.; Baer, L. M.; Pardi, A. *Nucleic Acids Res.* **1992**, *20*, 4507.
(23) Zhang, O.; Forman-Kay, J. D. *Biochemistry* **1995**, *34*, 6784.
(24) Kay, L. E.; Xu, G.-Y.; Singer, A. U.; Muhandiram, D. R.; Forman-Kay, J. D. *J. Magn. Res. Series B* **1993**, *101*, 333.
(25) Bax, A.; Clore, G. M.; Gronenborn, A. M. *J. Magn. Reson.* **1990**, *88*, 425.
(26) Santoro, J.; King, G. C. *J. Magn. Reson.* **1992**, *97*, 202.
(27) Vuister, G. W.; Bax, A. *J. Magn. Reson.* **1992**, *98*, 428.

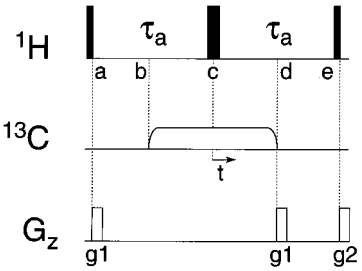

Figure 2. Purging scheme using a carbon WURST pulse[30,31] to minimize residual magnetization from protons attached to ^{13}C. Carbon magnetization is inverted at different times during the pulse in a manner dependent on the carbon chemical shift and the sweep rate of the WURST pulse (see Theory). The shape profile of the WURST pulse is given by eq 2, with apodization of the first and last 20% using a sine function.[31] The rate of the linear frequency sweep was optimized (see Table 1), so that at point *e* transverse magnetization arising from protons attached to ^{13}C is ideally completely antiphase, while ^{1}H magnetization from the non-^{13}C labeled component of the complex is in-phase. Gradients g1 eliminate artifacts created by imperfections in the ^{1}H 180° pulse applied in the center of the $2\tau_a$ period,[53] while g2 dephases magnetization originating from protons scalar coupled to ^{13}C.

nonconstant time HSQC experiments. The HCCH-TOCSY data set was recorded as described previously.[24] Samples of ^{15}N,^{13}C labeled N$^{1-22}$/unlabeled *boxB* RNA or unlabeled N$^{1-22}$/^{15}N,^{13}C labeled *boxB* RNA were employed for the coupling measurements. The sequence composition of the N$^{1-22}$ peptide (see above) is not representative of proteins in general, and data from the N$^{1-22}$/*boxB* RNA complex was supplemented by couplings measured from the drkN SH3 and PLCC SH2 domains. A curve describing the correlation of $^1J_{HC}$ values with carbon chemical shifts (δ_C, ppm) in proteins was obtained by weighting the contribution of each amino acid by its average occurrence in proteins[28] and subsequently scaling the weight of each $^1J_{HC}$ value by the frequency that it occurs within a given residue [i.e., in the case of Val $^1J_{HC}$ (methyl) is weighted six times more than $^1J_{HC}$ (alpha)]. The relation between $^1J_{HC}$ and δ_C for RNA was generated exclusively from couplings and chemical shifts measured from *boxB* RNA in complex with N$^{1-22}$. A fit of the $^1J_{HC}$ coupling/chemical shift data tabulated by Varani *et al.*[29] gave very similar results (see legend to Figure 1). Note that the $^1J_{HC}$ vs chemical shift relation will vary between molecules in a manner which depends on residue composition and to a smaller extent on secondary structure.

All NMR experiments were performed either at 25 °C (N$^{1-22}$/*boxB* RNA complex, drkN SH3) or 30 °C (PLCC SH2, dNumb PTB) on a Varian 500 MHz Inova spectrometer equipped with a pulsed field gradient unit and a triple resonance probe with an actively shielded z gradient. A 150 ms 3D ^{13}C F$_1$-filtered, F$_3$-edited NOESY experiment was recorded on a 3.0 mM sample of unlabeled N$^{1-22}$/^{15}N,^{13}C labeled *boxB* RNA dissolved in D_2O (see above for buffer conditions) at 500 MHz. A data matrix consisting of 100, 32, and 416 complex points in each of t_1, t_2, and t_3 was acquired; spectral widths of (3200, 3000, 8000 Hz) were recorded in each of F$_1$, F$_2$, and F$_3$ corresponding to (t_1, t_2, t_3) acquisition times of (31.3 ms, 10.7 ms, 52.0 ms). A relaxation delay of 1 s was employed along with 16 scans per FID to give a total acquisition time of approximately 70 h. A value of $\tau_a = 1.7$ ms was employed (see Figure 3a); WURST pulses[30,31] for purging had a sweep of 50 kHz, a sweep rate of 2.72×10^7 Hz/s (upfield to downfield), and a pulse width of 1.839 ms with the center of the frequency sweep at 50 ppm. All other experimental details are as described in the legend to Figure 3.

All spectra were processed on SUN SparcStations using NMRPipe/NMRDraw software[32] and analyzed using the program NMRView.[33] In the case of the 3D ^{13}C F$_1$-filtered, F$_3$-edited NOESY each of the dimensions was apodized with a 65° shifted squared sine-bell window function, zero filled (once), Fourier transformed, phased, and the imaginaries were eliminated. The absorptive part of the data set consisted of $256 \times 64 \times 1024$ real points.

Theory

Figure 1 shows the relation between the one bond ^{1}H−^{13}C scalar coupling, $^1J_{HC}$ (Hz), and carbon chemical shift (δ_C, ppm) for *boxB* RNA and a "standardized" protein where each residue is weighted according to its average frequency of occurrence in proteins (see Materials and Methods). A linear fit of $^1J_{HC}$ vs δ_C gives

$$^1J_{HC} = A\delta_C + B \qquad (1)$$

where (A, B) = (0.710 ± 0.037 Hz/ppm, 101.0 ± 3.5 Hz) and (0.365 ± 0.010 Hz/ppm, 120.0 ± 0.5 Hz) for RNA and protein, respectively. Correlation coefficients of 0.86 and 0.83, respectively, were obtained. It is clear that, for the most part, $^1J_{HC}$ increases with δ_C, and it is this correlation which forms the basis of the filtering methods proposed.

Figure 2 illustrates the basic pulse sequence element which is used to purge magnetization from protons coupled to ^{13}C spins. Central to this approach is the use of a frequency swept adiabatic ^{13}C inversion pulse. The utility of adiabatic pulses in this application can be appreciated by considering an accelerating (or decelerating) reference frame that rotates at the same frequency as the frequency swept carbon pulse.[34] For a sweep rate that is small compared to the appropriate effective field for the carbon spins, the trajectory of carbon magnetization follows the effective field for the duration of the pulse.[35] Thus if the carrier frequency of the pulse is initially far off resonance (for example, upfield of the signals of interest) and is swept through resonance and subsequently off resonance downfield of the signals, it is possible to completely invert the magnetization, in a manner which is very tolerant to B_1 inhomogeneity. Note that the effective field for carbons resonating at distinct frequencies will be different and such carbons will be largely inverted (0.8 M_z to −0.8 M_z) at different times, in a manner dependent on their frequency difference and the sweep rate and duration of the adiabatic inversion pulse. As an example, consider two carbon spins with one of the spins (spin A) located at the center of the frequency sweep, while the other spin (spin B) resonates 10 kHz downfield of A. Solution of the Bloch equations obtained by numerical integration shows that for an inversion pulse with a sweep of 60 kHz (upfield to downfield) and a duration of 2 ms, spin A will be inverted (0.8 M_z to −0.8 M_z) 0.33 ms prior to spin B. It is noteworthy that the difference in time between inversion of spins A and B is exactly what is calculated under the assumption that inversion occurs precisely when the frequency of the pulse coincides with the resonance frequency of the spin in question. Furthermore, the calculation shows that the time for inversion is 0.43 ms; although the assumption of instantaneous inversion is clearly not correct, it will be used as the starting point in our description since it provides a very simple intuitive base to understand the action of these pulses. Subsequently a quantum mechanical description will be provided.

Recently Böhlen and Bodenhausen[31] and Kupce and Freeman[30] have described an adiabatic pulse for wideband inversion. The rf is frequency swept and of constant amplitude, ω_1^{max}, throughout the duration of the majority of the pulse with the exception of the edges, where the B_1 field is ramped from zero

(28) Doolittle, R. F. *Predictions of Protein Structure and the Principles of Protein Conformation*; Plenum Press: 1989.
(29) Varani, G.; Tinoco, I., Jr. *J. Am. Chem. Soc.* **1991**, *113*, 9349.
(30) Kupce, E.; Freeman, R. *J. Magn. Reson. Ser. A* **1995**, *115*, 273.
(31) Bohlen, J. M.; Bodenhausen, G. *J. Magn. Reson. Ser. A* **1993**, *102*, 293.
(32) Delaglio, F.; Grzesiek, S.; Vuister, G. W.; Zhu, G.; Pfeifer, J.; Bax, A. *J. Biomol. NMR* **1995**, *6*, 277.
(33) Johnson, B. A.; Blevins, R. A. *J. Biomol. NMR* **1994**, *4*, 603.
(34) Böhlen, J.-M.; Burghardt, I.; Rey, M.; Bodenhausen, G. *J. Magn. Reson.* **1990**, *90*, 183.
(35) Freeman, R. *A Handbook of Nuclear Magnetic Resonance*; John Wiley & Sons: New York, 1988.

to $\omega_1{}^{max}$ and from $\omega_1{}^{max}$ to zero during the first and last fractions of the pulse (≈20%), respectively. These so called WURST pulses are superior to their frequency swept but B_1-constant counterparts. In the case of WURST pulses the magnetization is placed along the $-z$-axis at the end of inversion, while in the case of a pulse of constant B_1 field the effective field and hence the magnetization is never perfectly aligned along $-z$, even for very large frequency sweeps. With this in mind, we have chosen to employ WURST pulses for carbon broadband inversion with a shape amplitude defined by

$$\begin{aligned}\omega_1(n) &= \omega_1{}^{max}\sin\{(n\pi)/(2f)\}, \quad 1 \le n < f \\ &= \omega_1{}^{max}, \quad f \le n \le np - f \\ &= \omega_1{}^{max}\sin\{\pi/2+\pi/2[n-(np-f)]/f\}, \\ &\qquad np - f < n \le np \end{aligned} \tag{2}$$

where f/np corresponds to the fraction of the pulse during which the B_1 field is ramped up or down and np is the number of points in the pulse.

The basic purge element illustrated in Figure 2 consists of a spin echo period of duration $2\tau_a$, during which ^{1}H magnetization excited by the first 90° pulse is allowed to evolve due to the ^{1}H−^{13}C scalar coupling. Proton chemical shift evolution is refocused by the action of the ^{1}H 180° pulse at the center of the $2\tau_a$ period and can therefore be neglected. In what follows, we initially consider instantaneous carbon inversion occurring at the on-resonance condition, as discussed above. For a ^{1}H−^{13}C pair, where the ^{13}C spin is inverted at a time t, $t \ge 0$ after application of the ^{1}H 180° pulse, it can be shown that the evolution due to $^1J_{HC}$ occurs for a net time of $2\tau_a - 2t$. Thus, if the initial proton magnetization is along the y-axis, evolution between points a and e in the scheme of Figure 2 gives

$$I_y \xrightarrow{^1J_{HC}} I_y\cos[\pi{}^1J_{HC}(2\tau_a-2t)] - 2I_xC_z\sin[\pi{}^1J_{HC}(2\tau_a-2t)] \tag{3}$$

where I_i and C_i are the i ($i = x,y,z$) components of proton and carbon magnetization, respectively. Note that for each (I, C) pair there will be a different expression describing the evolution of I_y since the values of t and $^1J_{HC}$ will vary for each distinct carbon chemical shift. At point e in the sequence (at the end of the spin echo delay) maximum purging will occur if the coefficient of I_y in eq 3 is zero (coefficient of $2I_xC_z$ is ±1) for all protons coupled to ^{13}C spins. Subsequently, the antiphase magnetization from protons coupled to ^{13}C, $2I_xC_z$, is eliminated by the action of gradient g2 in the scheme of Figure 2. In contrast, proton magnetization from the unlabeled component of the complex is placed along the z-axis by the 90° pulse at point e and is unaffected by the gradient g2. The elimination of I_y (eq 3) requires that the relation

$$2\tau_a - 2t = \frac{2k+1}{2{}^1J_{HC}} \quad k = 0,1,2,... \tag{4}$$

hold for all values of t and $^1J_{HC}$ (*i.e.*, for all carbon spins). Because of finite proton transverse relaxation times it is necessary to choose $k = 0$. Since $t \ge 0$ and $^1J_{HC}$ is smallest for carbon spins resonating in the upfield portion of the carbon spectrum, upfield resonating carbons (for example, methyl carbons) must be inverted first, with frequency sweeping of the carbon inversion pulse proceeding in a downfield direction. Note that inversion of methyl carbons must occur close to $t = 0$ to minimize the value of τ_a.

The instantaneous frequency of the carbon transmitter, $\delta_{rf}(t)$, must be adjusted so that at time t, $\delta_{rf}(t) = \delta_C$ satisfies simultaneously eqs 1 and 4. We can write therefore that

$$2\tau_a - 2t = \frac{1}{2(A\delta_{rf} + B)} \tag{5}$$

where $k = 0$ has been chosen (see eq 4). The requisite sweep rate of the carbon transmitter during the WURST pulse can be obtained by taking the time derivative of both sides of eq 5 to give

$$A\frac{d\delta_{rf}}{dt} = 4(A\delta_{rf} + B)^2 \tag{6}$$

from which it follows that

$$\delta_{rf}(t) = \frac{J_0/A}{1 - 4J_0t} - \frac{B}{A} \quad t \ge 0 \tag{7}$$

where $J_0 = A\delta_{rf}(0) + B$, $\delta_{rf}(0)$ is the frequency position of the carbon carrier at $t = 0$, and J_0 is the $^1J_{HC}$ value for a carbon spin resonating at $\delta_C = \delta_{rf}(0)$. Equation 7 indicates that the optimum $\delta_{rf}(t)$ profile for a linear $^1J_{HC}$ vs carbon chemical shift profile is hyperbolic. Note that the procedure for calculating the best sweep rate for the carbon inversion pulse does not require that a linear coupling vs chemical shift relation hold; any functional relation between $^1J_{HC}$ and δ_C suffices.

While the qualitative features of the above discussion are correct and provide an intuitive understanding of the action of the scheme of Figure 2, a more rigorous description is necessary. This can be accomplished by using the Liouville−von Neumann equation

$$\frac{d\rho(t)}{dt} = i[\rho(t),H(t)] \tag{8}$$

where $\rho(t)$ is the density matrix and H(t) is the Hamiltonian for the system.[36,37] We can express the time-dependent Hamiltonian in the rotating frame that is synchronized with the instantaneous frequency of the carbon transmitter as

$$\begin{aligned} H_1(t) &= \omega_I I_z + 2\pi{}^1J_{HC}I_zC_z, \quad a \le t < b,\ d < t \le e \\ H_2(t) &= \omega_I I_z + [\omega_C - \omega_{rf}(t)]C_z + 2\pi{}^1J_{HC}I_zC_z + \omega_{1,C}(t)C_x, \\ &\qquad b \le t < c,\ c < t \le d \\ H_3(t) &= \omega_I I_z + [\omega_C - \omega_{rf}(t)]C_z + 2\pi{}^1J_{HC}I_zC_z + \omega_{1,C}(t)C_x + \\ &\qquad \omega_{1,I}I_x, \quad t = c \end{aligned} \tag{9}$$

where ω_I and ω_C are the Larmor frequencies of the proton and carbon spins, respectively, $\omega_C - \omega_{rf}(t)$ is the offset of the carbon spin with respect to the time-dependent carbon transmitter frequency, $\omega_{1,j}$ is the field strength of the ^{1}H ($j = I$) or ^{13}C ($j = C$) rf and the ^{1}H 180° pulse is applied instantaneously at $t = c$ (see Figure 2). Note the explicit time dependence of $\omega_{1,C}(t)$ in eq 9, as described by eq 2. Finally, the effects of the gradient pulses g1 have been neglected in eq 9 since they only serve to eliminate artifacts unrelated to purging.

Equation 8 is readily solved with $H_1(t)$, $a \le t < b$, $d < t \le e$, since the Hamiltonian is time independent. In the case of the other time periods, however, the Hamiltonian varies in time

(36) Slichter, C. P. *Principles of Magnetic Resonance*; Springer-Verlag: New York, 1980.

(37) Ernst, R. R.; Bodenhausen, G.; Wokaun, A. *Principles of Nuclear Magnetic Resonance in One and Two Dimensions*; Oxford University Press: Oxford, 1987.

and the evolution of $\rho(t)$ given by

$$\rho(t+\Delta t) = \exp[-iH(t)\Delta t]\rho(t)\exp[iH(t)\Delta t] \quad (10)$$

is valid only for very small time steps, Δt, where the Hamiltonian is to an excellent approximation constant. Thus, calculation of the evolution of $\rho(t)$ during the carbon adiabatic pulse is extremely time consuming since the Hamiltonian must be diagonalized for each interval Δt. Since the goal is to optimize the sweep rate, $\omega_{rf}(t)$, to achieve maximum suppression levels of magnetization originating from protons bound to ^{13}C carbons, it is necessary to repeat the calculations for different values of ω_C and finally for a large range of sweep rates. With this in mind, an alternative computationally much less intensive approach has been developed which relates $\rho(t+\Delta t)$ to $\rho(t)$ through a series of mathematical relations.

Consider, for example, the time interval $b \le t < c$ in Figure 2 during which the time dependent $H_2(t)$ is operative. Dividing this interval into a series of K equal steps of duration Δt where $\Delta t = (c-b)/K$ and j is an integer such that $1 \le j \le K$, we can write

$$\rho(j+1) = \exp[-iH(j+1)\Delta t]\rho(j)\exp[iH(j+1)\Delta t] \quad (11)$$

where $H(j+1)$ is the value of the Hamiltonian, $H_2(t)$, during the $j+1$ interval, and $\rho(j)$ and $\rho(j+1)$ are the values of the density matrix at the conclusion of the j and $j+1$ intervals, respectively (*i.e.*, at times of $j\Delta t$ and $[j+1]\Delta t$ after the start of the carbon pulse). Note that the delay Δt is chosen to be sufficiently small such that $H(j+1)$ is time independent. In order to evaluate eq 11, we transform the Hamiltonian into a tilted frame with the z-axis of this new frame aligned along the effective field. Noting that the effective field for the $j+1$ interval is the vector sum of the residual Zeeman field of magnitude $[\omega_C - \omega_{rf}(j+1)]$ and the ^{13}C rf field along the x-axis, $\omega_{1,C}(j+1)$, the transformation is accomplished by the operator, $\exp(i\theta_{j+1}C_y)$, which rotates the original frame by an angle θ_{j+1} about the y-axis. In the operator $\exp(i\theta_{j+1}C_y)$, θ_{j+1} is the angle that the effective field makes with respect to the z-axis of the accelerating frame during the $j+1$ interval. In this new frame, as we show below, the Hamiltonian, H_{eff} is diagonal, allowing a simple analytical expression describing evolution. Finally, the density matrix is rotated back to the original frame. Thus,

$$\rho(j+1) = \exp(-i\theta_{j+1}C_y)T(j+1)\exp(i\theta_{j+1}C_y)\rho(j) \times \exp(-i\theta_{j+1}C_y)T^{-1}(j+1)\exp(i\theta_{j+1}C_y) \quad (12.1)$$

where

$$T(j+1) = \exp(i\theta_{j+1}C_y)\exp[-iH(j+1)\Delta t]\exp(-i\theta_{j+1}C_y) \quad (12.2)$$

and

$$\tan\theta_{j+1} = \frac{\omega_{1,C}(j+1)}{\omega_C - \omega_{rf}(j+1)} \quad (12.3)$$

The operator $T(j+1)$ can be written as

$$T(j+1) = \exp(-iH_{eff}(j+1)\Delta t) \quad (13.1)$$

where

$$H_{eff}(j+1) = \omega_{eff}(j+1)C_z + 2\pi^1 J_{HC} I_z C_z \cos\theta_{j+1} - 2\pi^1 J_{HC} I_z C_x \sin\theta_{j+1} \quad (13.2)$$

and

$$\omega_{eff}(j+1) = \sqrt{[\omega_{1,C}(j+1)]^2 + [\omega_C - \omega_{rf}(j+1)]^2} \quad (13.3)$$

The third term in eq 13.2 does not commute with the first two and can be neglected without error because $\omega_{eff} \gg 2\pi^1 J_{HC}$; this has been confirmed with density matrix calculations. Note that the proton rf carrier is assumed to be on resonance ($\omega_I = 0$) in eq 13; in any event the spin echo period of the scheme of Figure 2 refocuses ^{1}H chemical shift.

It can be shown using eqs 12 and 13 that, assuming a density matrix of the form $\rho = A_0 I_y - B_0 2I_x C_z$ at point b in the sequence of Figure 2 (*i.e.*, immediately prior to the start of the carbon pulse), the value of the density matrix at the end of the jth interval of the carbon pulse, $\rho(j)$, for a two-spin ^{1}H$-^{13}$C spin system is given by

$$\rho(j) = A_j I_y - B_j 2I_x C_z - C_j 2I_x C_x - D_j 2I_x C_y \quad (14)$$

An evaluation of eq 12 using eq 13 shows that

$$\rho(j+1) = A_{j+1} I_y - B_{j+1} 2I_x C_z - C_{j+1} 2I_x C_x - D_{j+1} 2I_x C_y \quad (15)$$

where

$$A_{j+1} = A_j \cos(\beta_{j+1}) - [B_j \cos(\theta_{j+1}) + C_j \sin(\theta_{j+1})]\sin(\beta_{j+1})$$

$$B_{j+1} = \Lambda \cos(\theta_{j+1}) - [\Gamma \cos(\alpha_{j+1}) - D_j \sin(\alpha_{j+1})]\sin(\theta_{j+1})$$

$$C_{j+1} = \Lambda \sin(\theta_{j+1}) + [\Gamma \cos(\alpha_{j+1}) - D_j \sin(\alpha_{j+1})]\cos(\theta_{j+1})$$

$$D_{j+1} = \Gamma \sin(\alpha_{j+1}) + D_j \cos(\alpha_{j+1})$$

$$\alpha_{j+1} = \omega_{eff}(j+1)\Delta t$$

$$\beta_{j+1} = \pi^1 J_{HC} \cos(\theta_{j+1})\Delta t$$

$$\Lambda = A_j \sin(\beta_{j+1}) + [B_j \cos(\theta_{j+1}) + C_j \sin(\theta_{j+1})]\cos(\beta_{j+1})$$

$$\Gamma = -B_j \sin(\theta_{j+1}) + C_j \cos(\theta_{j+1}) \quad (16)$$

Equation 16 indicates that from the values of the coefficients of the density operator at the start of the carbon inversion pulse it is possible to calculate in an efficient manner the elements of the density operator at some later time. Equations for CH_n ($n > 1$) spin systems are more complex and are not given here. However, it is noteworthy that sweep rates obtained on the basis of eq 16 or from more complex calculations which explicitly include the number of protons coupled to a given carbon are identical. Note that the effect of the proton 180° pulse at point c in the sequence of Figure 2 is included simply by inverting the sign of magnetization proportional to I_y (the first term of eq 15) prior to continuing with the iterative scheme outlined above. It is clear from eq 15 that a classical description of the effect of the WURST pulse on a coupled system is not adequate, since multiple quantum terms are generated. Simulations have shown that the net effect of the creation of such terms is to decrease the rate at which in-phase magnetization, I_y, is transformed into antiphase signal, $2I_xC_z$, with the exact details varying in a manner dependent on the sweep rate employed, the position of the carbon spin in question, and the magnitude of the ^{1}H$-^{13}$C coupling.

Results and Discussion

Optimization of the Sweep Rate of the WURST Inversion Pulse. A number of different WURST frequency sweep profiles

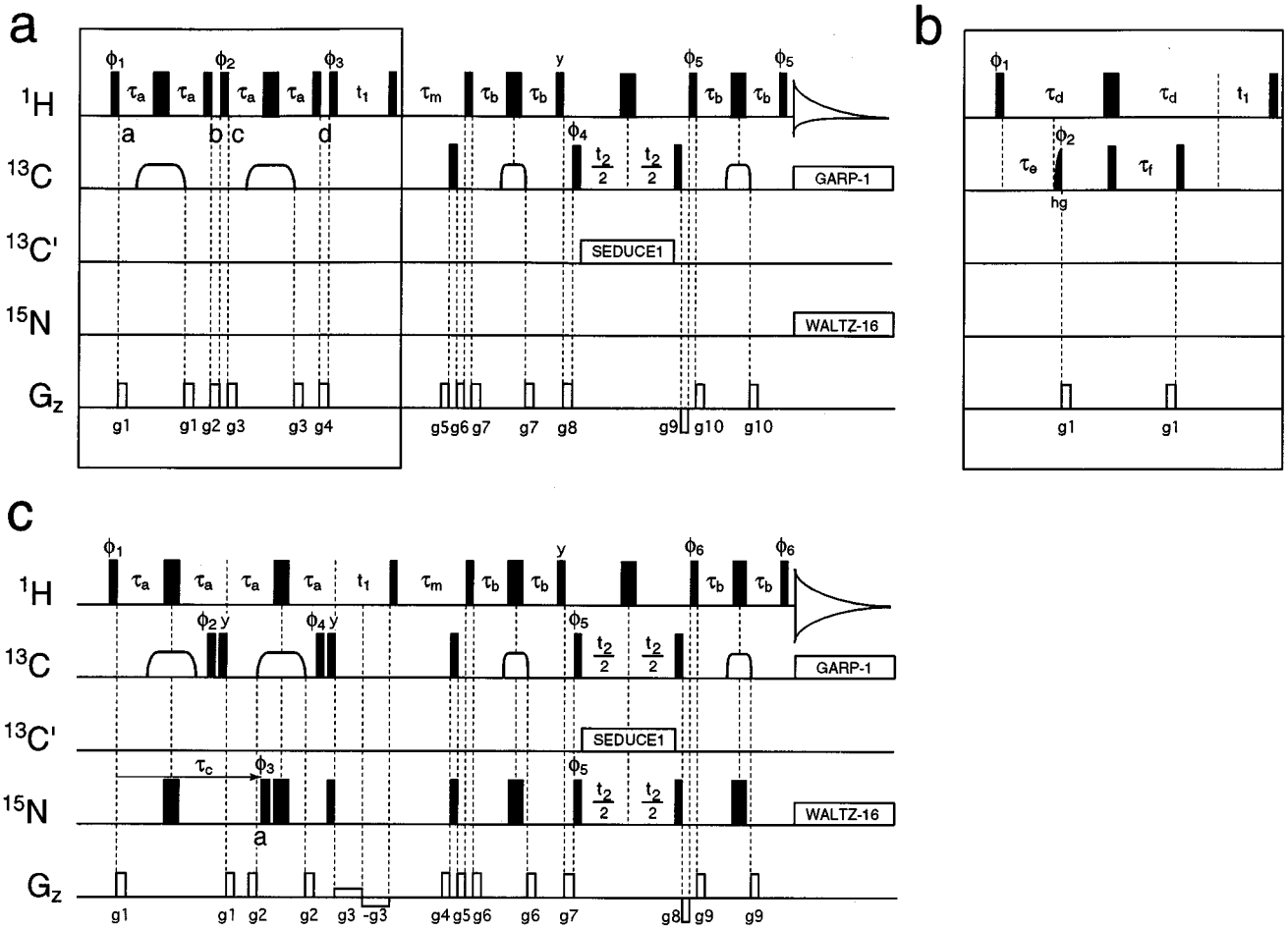

Figure 3. Pulse sequences for 3D ^{13}C F_1-filtered, F_3-edited NOESY-HSQC experiments for detection of intermolecular NOEs in D_2O (a,b) and H_2O (c) samples. All narrow (wide) pulses have flip angles of 90° (180°). The first two carbon pulses in (a), the first and fourth carbon pulses in (c), and the carbon pulses in the center of the INEPT[39] and reverse-INEPT periods in each of the sequences have the WURST profile[30,31] (see eq 2). All rectangular ^{1}H and ^{13}C pulses are applied with 28 and 21 kHz fields, respectively. (a) WURST-based pulse sequence optimized for a D_2O sample. Quadrature detection in t_1 and t_2 is achieved via States-TPPI[54] of ϕ_3 and ϕ_4, respectively. The phase cycling employed is as follows: $\phi_1 = (x,-x)$; $\phi_2 = 2(x), 2(-x)$; $\phi_3 = 4(x), 4(-x)$: $\phi_4 = 8(x), 8(-x)$; $\phi_5 = 2(x), 2(y)$; rec = $(x, -x, y, -y, -x, x, -y, y, -x, x, -y, y, x, -x, y, -y)$. The duration and strength of the gradients are g1 = (300 μs, 4 G/cm); g2 = (1 ms, 11 G/cm); g3 = (200 μs, 7 G/cm); g4 = (1 ms, 7 G/cm); g5 = (3 ms, 15 G/cm); g6 = (300 μs, 20 G/cm); g7 = (100 μs, 1 G/cm); g8 = (500 μs, 5 G/cm); g9 = (500 μs, −7 G/cm); g10 = (300 μs, 20 G/cm). *Application to ^{13}C labeled RNA samples:* The ^{1}H carrier is centered at 4.77 ppm. The carbon carrier is positioned at 110 ppm, and the first two WURST pulses are applied with a 50 kHz frequency sweep (500 and 600 MHz, see Table 1), with the center of the pulse at 50 ppm (*i.e.*, approximately 10 ppm upfield of the start of the carbon spectrum). The frequency is swept from upfield to downfield, with a rate given in Table 1. Note that the τ_a value is adjusted according to the sweep rate chosen, as indicated in Table 1. The center of each of the WURST pulses corresponds to the point of application of the ^{1}H 180° pulse in the middle of the $2\tau_a$ period. Each of the WURST pulses in the purging elements is applied with a $B_{1,max}$ of 5 kHz. The final two WURST pulses are of duration 500 μs, are centered at 110 ppm, have sweep widths of 50 kHz (linear sweep rate of 1.0×10^8 Hz/s; upfield to downfield), and employ an 8.4 kHz rf field. These WURST pulses are used for broadband inversion during the INEPT and reverse-INEPT sequences. Carbonyl decoupling is not employed. Decoupling during acquisition is achieved with a 2.9 kHz GARP-1 field[55] (^{13}C) and an 800 Hz WALTZ-16 field[56] (^{15}N, centered at 160 ppm). The value of τ_b is set to 1.6 ms. *Application to ^{13}C labeled protein samples:* ^{1}H and ^{13}C rectangular pulses are centered at 4.73 and 67.0 ppm, respectively. The first two WURST pulses (60 kHz sweep at 500 and 600 MHz; upfield to downfield) are centered at 0 ppm and employ a 5 kHz field. Table 1 lists optimized values for the sweep rate and τ_a. The final two WURST pulses ($B_{1,max}$ = 8.4 kHz) are of duration 500 μs and employ a 60 kHz sweep range using a linear sweep rate of 1.2×10^8 Hz/s centered at 67 ppm. The value of τ_b is set to 1.7 ms. Carbonyl decoupling is achieved by 109 ppm cosine modulation of a WALTZ-16 sequence[57] with pulses having the SEDUCE-1 profile[58] (320 μs 90° pulse, 1.7 kHz peak amplitude). ^{13}C decoupling during acquisition uses a 3.7 kHz GARP-1 field.[55] ^{15}N decoupling is not employed. (b) Same pulse sequence as in (a) except for the filtering scheme (boxed region). In this case, the magnetization is purged using a triple purge scheme involving ^{13}C 90° pulses, as described in the text. This scheme is not as efficient as the sequence in (a) but is included for comparison. Quadrature in F_1 is obtained by States-TPPI[54] of $\phi 1$. The phase cycling employed is as follows: $\phi_1 = 4(x),4(-x)$; $\phi_2 = (x,-x)$; $\phi_4 = 8(x),8(-x)$; $\phi_5 = 2(x),2(y)$; rec = $2(x),2(-y),2(-x),2(y),2(-x),2(y),2(x),2(-y)$. The duration and strength of the gradients are the same as in (a) except for g1 = (400 μs, 12 G/cm). *Application to ^{13}C labeled RNA samples:* The ^{13}C rectangular pulses are initially centered at 85 ppm, with the carbon carrier jumped to 110 ppm at the end of the mixing period. The half-Gaussian pulse[59] (380 μs; maximum rf amplitude of 1.58 kHz), denoted by hg, is included to suppress magnetization originating from aromatic protons. The pulse is centered at 145 ppm using 60 ppm phase modulation of the carbon carrier.[60,61] The values of τ_d and τ_f were set to 3.45 and 2.78 ms, respectively, while τ_e was optimized to 1.6 ms by minimizing residual proton magnetization from aromatic residues in the first t_1 point of a short mixing time (10 ms) NOESY. The value of τ_e should be optimized for each sample. *Application to ^{13}C labeled protein samples:* High power carbon pulses are centered at 43 ppm; the carbon carrier is jumped to 67 ppm at the end of the mixing period, τ_m. The half-Gaussian pulse[59] (hg) is centered at 130 ppm using an 87 ppm phase modulated pulse.[60,61] The values of τ_d, τ_e, and τ_f were set to 4.0, 2.0, and 3.57 ms, respectively. The value of τ_e was obtained experimentally by minimizing the residual signal from aromatic protons in the first block of a short mixing time NOESY. (c) WURST-based pulse scheme optimized for H_2O samples. Many of the details of the sequence are as described in (a); only the differences are discussed here. NOEs from the unlabeled component to either NH or CH protons of the labeled molecule are observed. The simultaneous ^{15}N and ^{13}C pulses are applied as described previously.[62] The value of τ_b is optimized for the transfer between ^{1}H and ^{13}C. The value of τ_c is set to $1/(2J_{HN})$. Quadrature in F_1 and F_2 is obtained by States-TPPI[54] of $\phi 1$ and $\phi 5$, respectively. The phase cycle employed is as follows: $\phi_1 = 4(x+135°),4(-x+135°)$; $\phi_2 = \phi 3 = (x,-x)$; $\phi_4 = 2(x),2(-x)$; $\phi_5 = 8(x),8(-x)$; $\phi 6 = 2(x),2(y)$; rec = $2(x),2(-y),2(-x),2(y),2(-x),2(y),2(x),2(-y)$. The duration and strength of the gradients are g1 = (300 μs, 12 G/cm); g2 = (200 μs, 15 G/cm); g3 = (t_1/2, 2 G/cm); g4 = (3 ms, 15 G/cm); g5 = (300 μs, 20 G/cm); g6 = (100 μs, 3 G/cm); g7 = (4 ms, 30 G/cm); g8 = (3 ms, −18 G/cm); g9 = (300 μs, 20 G/cm). All ^{15}N pulses are applied with a 6.3 kHz field. For applications to labeled RNA, the ^{15}N carrier is positioned at 117 ppm, and ^{15}N decoupling during acquisition is achieved using a 1.3 kHz GARP-1 field.[55] In the case of applications to complexes with labeled protein, the ^{15}N carrier is placed at 110 ppm, and an 800 Hz GARP-1 decoupling field is employed.

Table 1. Optimized Sweep Rates $\dot{\nu}$ (Hz/s)[a] and τ_a Values (ms)[b] for the WURST Pulses Used in the Purging Schemes of Figures 2 and 3 Assuming a Linear Relation between $^1J_{HC}$ and δ_C (eq 1)

	RNA[c]						proteins[c]					
$\gamma\vec{B}_0/2\pi$[d] (MHz)	τ_a (ms)	$\Delta\Omega$[e] (kHz)	$\dot{\nu}$ (10^7 Hz s^{-1})	τ_p (ms)	ν_1^{max}[f] (kHz)	χ^2[g]	τ_a (ms)	$\Delta\Omega$[e] (kHz)	$\dot{\nu}$ (10^7 Hz s^{-1})	τ_p (ms)	ν_1^{max}[f] (kHz)	χ^2[g]
500	1.7	50	2.719	1.839	5	0.990	2.0	60	3.347	1.793	5	1.146
	1.8	50	2.194	2.279	5	0.996	2.1	60	2.644	2.269	5	0.754
							2.2	60	2.182	2.750	5	0.826
600	1.7	60	3.254	1.844	5	0.984	2.0	60	3.905	1.536	5	1.019
	1.8	60	2.565	2.339	5	1.071	2.1	60	3.087	1.944	5	0.725
							2.2	60	2.543	2.359	5	0.895
750	1.7	80	4.074	1.964	6	0.985	2.0	80	4.905	1.631	5	0.939
	1.8	80	3.213	2.490	6	1.079	2.1	80	3.850	2.078	5	0.720
							2.2	80	3.212	2.491	5	1.031
800	1.7	80	4.304	1.859	6	0.990	2.0	80	5.239	1.527	6	0.955
	1.8	80	3.393	2.358	6	1.092	2.1	80	4.107	1.948	5	0.725
							2.2	80	3.393	2.358	5	1.042

[a]

$$\dot{\nu} = \frac{d\nu_{rf}(t)}{dt} = \frac{1}{2\pi}\frac{d\omega_{rf}(t)}{dt} = \frac{\gamma_C}{\gamma_H}\frac{\gamma\vec{B}_0}{2\pi}10^{-6}\frac{d\delta_{rf}(t)}{dt}$$

where γ_i is the gyromagnetic ratio of spin i. [b] See Figures 2 and 3. [c] For RNA $^1J_{HC} = (0.710 \pm 0.037$ Hz/ppm$)\ \delta_C + 101.0 \pm 3.5$ Hz, while for proteins $^1J_{HC} = (0.365 \pm 0.010$ Hz/ppm$)\ \delta_C + 120.0 \pm 0.5$ Hz. [d] Field strength as measured by the ^{1}H resonance frequency. [e] Frequency sweep of the WURST pulse. The center of this pulse coincides with the ^{1}H 180° refocusing pulse (see Figures 2 and 3). At this point the carbon carrier is ≈10 ppm upfield of the first of the ^{13}C spins to be inverted. [f] $\nu_1^{max} = \omega_1^{max}/2\pi$ is the maximum rf field strength for the WURST pulses. [g] χ^2 values correspond to the residual transverse magnetization after the double purge scheme of Figure 3a, defined according to

$$\chi^2 = \sqrt{\sum_i (I_t^i)^2}$$

where I_t^i is the total transverse magnetization for the ith ^{1}H−^{13}C spin pair and the sum runs over all ^{1}H−^{13}C pairs given in Figures 1 (parts b and c). For each double purge element, identical evolution times and pulse durations were employed. At all magnetic fields, the best suppression in the case of protein−peptide complexes was obtained with "asymmetrical" double purges (of total durations τ_{ab} and τ_{cd}, respectively, where τ_{ij} is the time between points i and j in Figure 3a) consisting of an initial purge with an evolution time of 2 × 2.2 ms (τ_{ab}) and a second purge with an evolution time of 2 × 2.0 ms (τ_{cd}): $\chi^2 = 0.685$ at 500 MHz, $\chi^2 = 0.668$ at 600 MHz, $\chi^2 = 0.685$ at 750 MHz, and $\chi^2 = 0.698$ at 800 MHz.

have been examined and multispin effects taken into account by density matrix calculations using eqs 15 and 16 (i.e., describing all spins systems as CH). In all cases the amount of in-phase ^{13}C-coupled proton magnetization at the completion of the $2\tau_a$ period of Figure 2 (point *e*) was minimized by adjusting the sweep rate of the WURST pulse, its duration τ_p, and the delay τ_a using a SIMPLEX algorithm.[38] The simplest sweep profile is linear ($d\delta_{rf}(t)/dt$ = constant), and suppression levels achieved by linear frequency sweeps were initially examined. In all simulations a constant total sweep of either 50, 60, or 80 kHz was employed, and a linear relation between $^1J_{HC}$ and δ_C, given by the best linear fit of the experimental data in Figure 1, was assumed (eq 1). In addition, the maximum rf amplitude of the WURST pulse was set to 5 kHz ($\omega_1^{max}/2\pi$ = 5 kHz, see eq 2 and Table 1), above the critical rf threshold necessary to insure adiabatic inversion for all spins considered in the optimization procedure. Subsequently more complex $\delta_{rf}(t)$ profiles were studied as well, based on a starting function given by eq 7. Particularly outstanding suppression of in-phase proton magnetization can be achieved in this case for a $^1J_{HC}$ vs δ_C relation given by eq 1. However, when the range of $^1J_{HC}$ values observed experimentally for a given δ_C is considered (see Figure 1), adiabatic schemes based on linear frequency sweeps provide as good a level of suppression as achieved using pulses with more complex sweep profiles that have been examined. Therefore, results from linear sweeps only are presented in what follows. Table 1 lists optimal rates and values of τ_a and τ_p for a number of different magnetic field strengths and for the suppression of carbon bound protons in either proteins or RNA.

(38) Vetterling, W. T.; Press, W. H.; Teukolsky, S. A.; Flannery, B. R. *Numerical Recipes in C*; Cambridge University Press: Cambridge, 1988.

It is instructive to compare the optimal frequency sweep established from quantum mechanical calculations (Table 1) with rates predicted on the basis of purely classical arguments. In what follows we consider an example involving purging proton magnetization from ^{13}C labeled protein samples, although a similar scenario holds for labeled RNA applications as well. From eq 7 it follows that

$$\frac{d\delta_{rf}(t)}{dt} = \frac{\frac{4J_0^2}{A}}{(1 - 4J_0 t)^2} \qquad (17)$$

from which sweep rates of $4J_m^2/A$ ($\delta_{rf} \approx$ methyl region) and $4J_a^2/A$ ($\delta_{rf} \approx$ aromatic region) are calculated, where J_m and J_a are average ^{1}H−^{13}C coupling constants for methyl and aromatic carbons, respectively. The average sweep rate, $\langle d\delta_{rf}(t)/dt\rangle$, of the pulse between the methyl and aromatic regions is given by the geometric mean of the rates at the two extremes (methyls and aromatics), $4J_mJ_a/A \approx 2.9 \times 10^7$ Hz/s, for a spectrometer frequency of 500 MHz. In order to compare this value with the rates given in Table 1, we consider a sweep width of 60 kHz with the center of the WURST pulse at 0 ppm. It can be shown that for $A = 0.365$ Hz/ppm and $B = 120.0$ Hz (eq 1, protein applications) a pulse with a sweep rate defined by eq 17 will have a duration of ≈1.8 ms. The average sweep rate calculated based on a classical derivation (2.9×10^7 Hz/s) is therefore somewhat smaller than the rate calculated using the quantum mechanical approach outlined in Theory (see Table 1) for a pulse width of similar duration (3.3×10^7 Hz/s). As described above, the evolution of multiple quantum terms during the WURST pulse effectively decreases the rate at which in-phase magnetization evolves. To compensate for this decrease in rate, the time for evolution due to $^1J_{HC}$ must be increased.

This is accomplished through a faster frequency sweep so that the time between inversion of proton and carbon spins is decreased (see eq 4).

Experimental Pulse Schemes. Figure 3 illustrates the pulse schemes that have been developed for recording intermolecular NOEs in complexes consisting of both ^{15}N,^{13}C labeled and unlabeled components. The sequence of Figure 3a is optimized for samples dissolved in D_2O. The first part of the sequence consists of a pair of purging elements to suppress magnetization originating from protons coupled to ^{13}C. Each of these elements of duration $2\tau_a$, extending from *a* to *b* and from *c* to *d*, makes use of a WURST pulse as described above. The delay $2\tau_a$ is on the order of $1/(2^1J_{HC,min})$, where $^1J_{HC,min}$ is the smallest ^{1}H−^{13}C one-bond coupling value in the molecular complex considered (see Table 1), and is calculated via the optimization procedure discussed above. After chemical shift evolution during t_1, magnetization is transferred between proximal protons during the NOE mixing time, τ_m. Magnetization transferred to protons bound to ^{13}C is subsequently relayed from ^{1}H to ^{13}C via the INEPT scheme[39] that follows, ^{13}C chemical shift is recorded during t_2, and the signal transferred back to protons for detection. Note that WURST pulses are also used for ^{13}C broadband inversion in the INEPT transfers. However, because the delay $2\tau_b$ is chosen to be somewhat less than $1/(2^1J_{HC})$ to minimize relaxation losses, these pulses are applied with much shorter widths than their counterparts used for purging (duration of 400−500 μs), and no attempt to match the sweep rate with the $^1J_{HC}$ vs δ_C profile is made. Fourier transformation of the resultant data set gives rise to a spectrum with cross peaks at (ω_{Hi}, ω_{Cj}, ω_{Hj}), where H_i and H_j are dipolar coupled protons attached to unlabeled and ^{13}C labeled molecules, respectively. Note that a ^{13}C 180° pulse is not applied in the middle of the t_1 period so that signal from protons coupled to ^{13}C that escapes the filtering elements that precede t_1 evolution is allowed to evolve due to $^1J_{HC}$ during this period, giving rise to artifacts at ($\omega_{Hi} \pm \pi\, ^1J_{HC}$, ω_{Ci}, ω_{Hi}). By means of comparison, Figure 3b illustrates a filtering scheme that we had previously employed to measure intermolecular NOEs[16] based on the original sequence of Ikura and Bax.[5] A triple purge scheme was employed with an aromatic selective pulse centered at 130 ppm (145 ppm) for the suppression of aromatic protons arising from labeled protein (RNA) and a pair of ^{13}C nonselective 90° pulses applied at delays of τ_d and ($\tau_d + \tau_f$) from the start of evolution of proton magnetization, optimized for different values of $^1J_{HC}$.

Figure 3c illustrates the corresponding pulse sequence developed for application to molecular complexes dissolved in H_2O. With the exception of the ^{15}N pulses which filter/edit protons attached to ^{15}N, the "H_2O" and "D_2O" sequences are very similar. One difference, however, is that at the conclusion of the $2\tau_a$ period of each of the purging elements in the H_2O experiment (Figure 3c) proton magnetization is not returned to the +*z*-axis. This allows NH magnetization derived from the labeled component of the complex to continue to evolve due to the one-bond ^{15}N-NH scalar interaction so that at point *a* (corresponding to the delay τ_c) in the pulse scheme, amide magnetization is antiphase with respect to nitrogen and can be effectively purged by the application of an ^{15}N 90° pulse. Suppression of magnetization from protons coupled to ^{13}C spins is achieved in this case by a ^{13}C 90°−90° pulse pair, with phase cycling of the first 90° pulse. Magnetization not affected by the first of the two 90° ^{13}C purging pulses due to off-resonance effects will be purged by the action of the second pulse.

Figure 4 shows a comparison of the calculated suppression levels achieved using the purge schemes of Figure 3 (3a (boxed region) and 3b). Results for ^{1}H−^{13}C pairs in RNA and proteins are presented, assuming a linear relation between $^1J_{HC}$ and δ_C

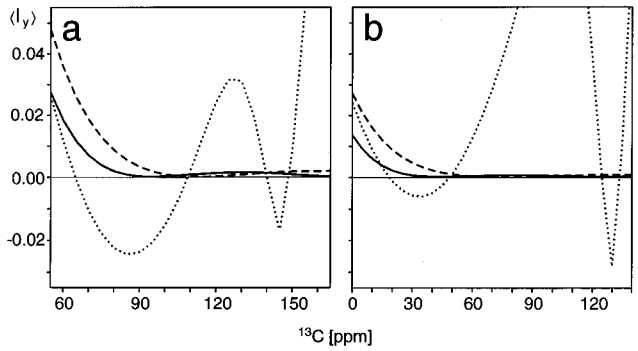

Figure 4. Comparison of residual in-phase magnetization, I_y, for protons one-bond coupled to ^{13}C, after the purging schemes of Figure 3 (parts a and b) (see boxed regions of Figure 3). The evolution of coherences during each of the purging elements was calculated using the product operator formalism[37,63] and simplifying the calculations by approximating all spin systems as CH (see eq 16). The simulations were carried out assuming a 500 MHz ^{1}H resonance frequency. RF offset effects were explicitly included in the calculations. Amplitudes and centers of excitation for all ^{13}C rf pulses are as described in the legend to Figure 3. (a) Curves calculated for RNA, with the $^1J_{HC}$ vs δ_C profile given by the relation $^1J_{HC} = 0.710$ Hz/ppm $\delta_C + 101$ Hz. *Dotted line:* Residual magnetization from protons coupled to ^{13}C after the purge scheme of Figure 3b. All the delays are as given in the legend to Figure 3b, with the exception of τ_e which was set to 1 ms, to minimize the residual magnetization from aromatic protons. *Dashed line:* Residual proton magnetization after the purge scheme of Figure 3a (*i.e.*, immediately before the t_1 period) using a WURST pulse[30,31] optimized for $\tau_a = 1.7$ ms (50 kHz sweep at a rate of 2.72×10^7 Hz/s; see Table 1). *Solid line:* Residual proton magnetization using the sequence of Figure 3a and a WURST pulse optimized for $\tau_a = 1.8$ ms (50 kHz sweep at a rate of 2.19×10^7 Hz/s; see Table 1). (b) Simulations for proteins calculated assuming the relation $^1J_{HC} = 0.365$ Hz/ppm $\delta_C + 120.0$ Hz. *Dotted line:* Residual magnetization after the purge scheme of Figure 3b, with all delays and rf powers as described in the legend to Figure 3 with the exception that τ_e is set to 1.2 ms in the present case. *Dashed and solid lines:* Residual proton magnetization after the WURST-based purge sequence of Figure 3a using a WURST pulse optimized for $\tau_a = 2$ ms (dashed; 60 kHz sweep at a rate of 3.35×10^7 Hz/s) and $\tau_a = 2.1$ ms (solid; 60 kHz sweep at a rate of 2.64×10^7 Hz/s). All the parameters defining the WURST pulses are given in Table 1.

(eq 1) which best fits the data illustrated in Figure 1. It is clear that significantly better results can be achieved using the WURST based approach. Unlike the hard pulse purge schemes which perform poorly in the aromatic region of the carbon spectrum in the case of proteins and in the aromatic and C1′/C5 regions in the case of RNA, the performance of the WURST-based suppression schemes are much less dependent on carbon chemical shift. Thus, it is not necessary to perform separate experiments optimized for either aliphatic- or aromatic-purging using the scheme of Figure 3 (parts a and c), while separate experiments might well be carried out if the sequence indicated in Figure 3b was employed. In addition, although off-resonance effects were included in all of the calculations in Figure 4, the effect of rf inhomogeneity, which will vary in a probe dependent manner, was not. One of the characteristics of adiabatic pulses is their insensitivity to rf inhomogeneity once a critical power level is achieved, and this is a particularly important feature in the present application where suppression levels of greater than 99% are desired.

Experimental verification of the WURST-based purging scheme is presented in Figure 5, where 10 ms mixing time NOE experiments are illustrated using the pulse schemes indicated in Figure 3 (parts a and b) with the delay t_2 set to zero and a ^{13}C refocusing pulse inserted in the middle of the t_2 period. For very short mixing time NOESY experiments diagonal peaks only are obtained centered at ($\omega_H \pm \pi^1J_{HC}$, ω_H), the result of

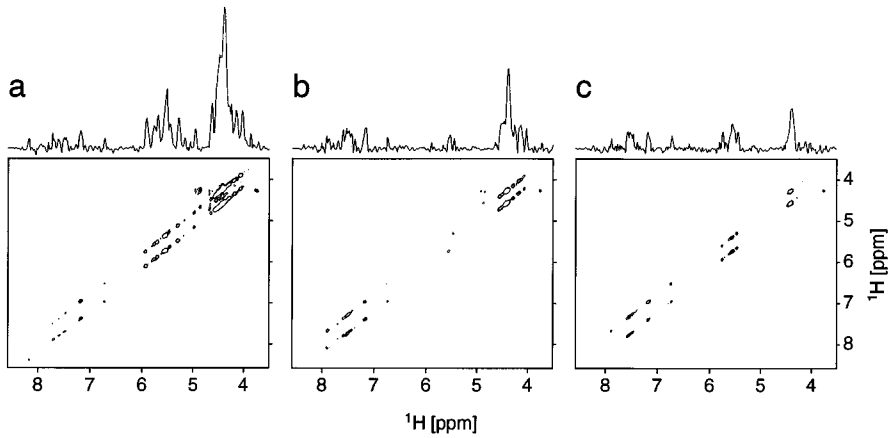

Figure 5. Improved filtering in 2D F_1-filtered, F_2-edited (^{1}H,^{1}H) NOESY-HSQC experiments of unlabeled $N^{1-22}/^{15}N$,^{13}C labeled *boxB* RNA. The spectra were collected at 500 MHz with mixing times of 10 ms. ^{1}H sweep widths of 8000 Hz (t_2) and 3800 Hz (t_1) were recorded with 416 and 128 complex points, respectively. A 1 s recycle delay was employed giving rise to an acquisition time of approximately 5 h/spectrum. (a) Spectrum obtained with the sequence of Figure 3, where the boxed region in Figure 3b replaces the scheme in the box of Figure 3a. All delays and field strengths are described in the legend to Figure 3. Note that the value of τ_e may vary with each sample. (b) WURST-purge experiments with the pulse sequence described in Figure 3a using a τ_a value of 1.7 ms. The WURST pulse used for purging ($B_{1,max} = 4.7$ kHz) covers a 50 kHz sweep range (upfield to downfield) in 1.839 ms using a linear sweep rate of 2.719×10^7 Hz/s centered at 50 ppm. (c) Same as (b), with the exception that a τ_a value of 1.8 ms is employed. The WURST pulse ($B_{1,max} = 4.7$ kHz) covers a 50 kHz sweep range in 2.279 ms using a linear sweep rate of 2.194×10^7 Hz/s centered at 50 ppm. In each of (a)−(c) a 1D projection of the data is shown at the top of each 2D spectrum. Each point of the projection was generated by summing the absolute value of signal intensity spanning ±120 Hz about the diagonal along F_1. All signal below three times the standard deviation of the noise was reduced by a factor of 4 in order to minimize the noise floor in each projection.

imperfect purging. The efficacy of a particular filtering scheme is therefore readily evaluated by inspection of short mixing time F_1-filtered, F_2-edited NOESY data sets for residual magnetization. Results on a 3.0 mM complex of unlabeled $N^{1-22}/^{15}N$,^{13}C labeled *boxB* RNA are presented. In Figure 5a the purging scheme of Figure 3b is employed (*i.e.*, purging achieved by hard ^{13}C 90° pulses), with the delay τ_e optimized experimentally to minimize signal from the aromatic residues. The results are compared with spectra obtained with the sequence of Figure 3a (WURST pulses) in Figure 5 (parts b ($\tau_a = 1.7$ ms, WURST sweep rate $= 2.72 \times 10^7$ Hz/s) and c ($\tau_a = 1.8$ ms, WURST sweep rate $= 2.19 \times 10^7$ Hz/s)), where it is clear that improved suppression levels are obtained. Note that both of the WURST pulses have been optimized in the manner described in the Theory section. The experimental results are in qualitative agreement with the relative suppression levels calculated in Figure 4. For example, the purging scheme with $\tau_a = 1.7$ ms, $d\nu_{rf}(t)/dt = 2.72 \times 10^7$ Hz/s, results in inferior suppression of signal from the H2′,H3′,H4′ and H5′/H5″ protons relative to the scheme with $\tau_a = 1.8$ ms and $d\nu_{rf}(t)/dt = 2.19 \times 10^7$ Hz/s, as calculated.

Figure 6 shows results from the corresponding experiments recorded on a 1.4 mM complex of an ^{15}N, ^{13}C labeled dNumb PTB domain and a 10 residue unlabeled peptide. Significantly improved suppression is achieved with the purging scheme employing WURST pulses (Figure 6 (parts b and c)) relative to the sequence employing hard ^{13}C 90° pulses for filtering (Figure 6a). We have also compared the scheme of Figure 3a with the sequence described by Ogura et al.[15] in which the frequency swept WURST pulses between points *a* and *b* and points *c* and *d* in Figure 3 are replaced by 360 μs WURST pulses. In this comparison only 1D spectra were recorded with a τ_m value set to 10 ms. Therefore, essentially no signal should be observed in spectra since the NOE mixing time is insufficient to allow magnetization transfer from peptide to protein. Figure 6d illustrates the spectrum obtained using the sequence proposed by Ogura et al.[15] with the delays for purging as suggested by this group (i.e., the delays between points *a* and *b* (τ_{ab}) and between *c* and *d* (τ_{cd}) are set to 2×1.85 and 2×1.45 ms, respectively). We were able to improve the performance of this sequence considerably by optimizing the purging delays ($\tau_{ab} = 2 \times 2.0$ ms and $\tau_{cd} = 2 \times 1.75$ ms), as shown in Figure 6e. However, the results obtained in Figure 6f illustrate that still further improvements can be obtained using WURST pulses with sweep rates adjusted to reflect the appropriate $^1J_{HC}$ vs chemical shift profile and that it is possible to effectively suppress magnetization arising from protons coupled to aromatic and aliphatic carbons in the same experiment.

The experimental results for both RNA and proteins establish that while the WURST schemes offer superior performance relative to the other sequences there is some variability in suppression levels depending on the values of τ_a and the sweep rates employed. For example, for applications to proteins the simulations in Figure 4b and the experiments of Figure 6 (parts b and c) establish that improved suppression of methyl protons is achieved using a WURST sweep rate of $d\nu_{rf}(t)/dt = 2.64 \times 10^7$ Hz/s ($\tau_a = 2.1$ ms) relative to a rate of 3.35×10^7 Hz/s ($\tau_a = 2.0$ ms). In contrast, the situation is reversed for protons attached to carbons resonating in the range of 40−60 ppm. The τ_a value (see sequences of Figures 2 and 3) and hence the sweep rate used in an experiment often represent a compromise between the desired level of purging and the signal losses that can be tolerated due to transverse relaxation of magnetization from the unlabeled component during the purging period. As noted in Table 1, simulations and experimental results establish that for purging signals arising from labeled protein the use of a double purge scheme with $\tau_{ab} = 2 \times 2.2$ ms and $\tau_{cd} = 2 \times 2.0$ ms offers optimal suppression levels. In this regard we have not observed any advantages in using such an asymmetric purging scheme for unlabeled peptide/labeled RNA samples (relative to sequences with $\tau_{ab} = \tau_{cd}$).

Application to the N^{1-22}/*boxB* RNA Complex. The bacteriophage λ N protein controls its gene expression by binding to antitermination signals (*nut* sites) on its mRNA.[40] Recognition of these control sites on mRNA by the N protein involves an arginine-rich motif that is a common element found in many RNA-binding proteins.[41] Three-dimensional structures of peptide-RNA complexes involving such motifs and RNA internal loops have been solved by heteronuclear NMR spectroscopy

(39) Morris, G. A.; Freeman, R. *J. Am. Chem. Soc.* **1979**, *101*, 760.
(40) Greenblatt, J.; Nodwell, J. R.; Mason, S. W. *Nature* **1993**, *64*, 401.
(41) Lazinski, D., Grzadzielska, E., Das, A. *Cell* **1989**, *59*, 207.

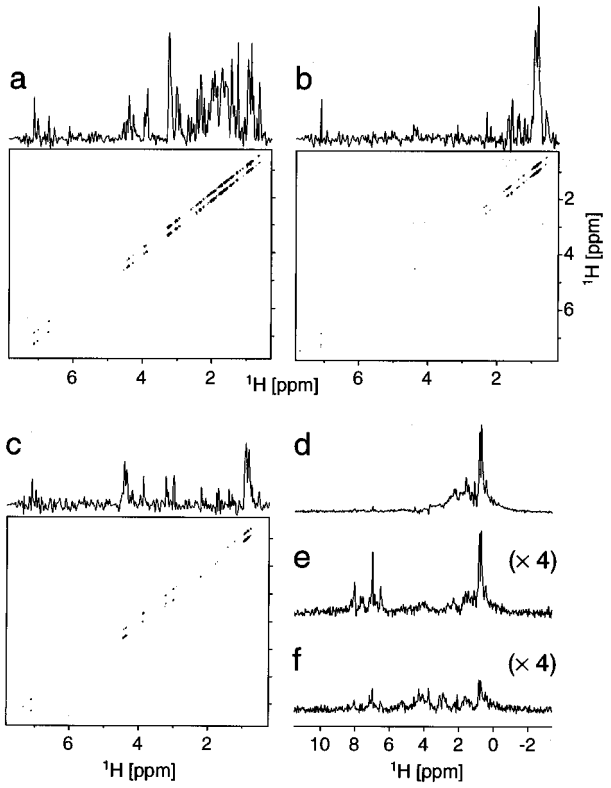

Figure 6. Improved filtering in F_1-filtered, F_2-edited (^{1}H,^{1}H) NOESY-HSQC experiments of the ^{15}N/^{13}C dNumb PTB domain complexed with a 10 residue peptide (see Materials and Methods). The spectra (500 MHz) were collected with mixing times of 10 ms. Spectral widths of 8000 Hz (t_2) and 3800 Hz (t_1) and were recorded with 416 and 128 complex points, respectively. A 1 s recycle delay was employed giving rise to an acquisition time of approximately 5 h/spectrum. In the case of 1D spectra 128 transients were acquired. (a) 2D spectrum obtained with the pulse sequence described in Figure 3b. All delays and rf levels of pulses are indicated in the legend to Figure 3. (b) 2D spectrum obtained using the scheme of Figure 3a employing a τ_a value of 2.0 ms and WURST pulses for purging centered at 0 ppm and covering a 60 kHz sweep range with a linear sweep rate of 3.347×10^7 Hz/s (pulse width = 1.793 ms; $B_{1,max}$ = 4.7 kHz). (c) As in (b) with the exception that a τ_a value of 2.1 ms was employed. Each of the WURST pulses employed in the purging scheme covers a 60 kHz sweep range in 2.269 ms using a linear sweep rate of 2.644×10^7 Hz/s centered at 0 ppm ($B_{1,max}$ = 4.7 kHz). Projections were generated in the manner described in the legend to Figure 5. (d) 1D spectrum obtained by replacing the frequency swept WURST pulses adjusted to the $^1J_{HC}$ vs chemical shift profile between points *a* and *b* and points *c* and *d* in the sequence of Figure 3a with 360 μs WURST pulses (11.4 kHz) centered at 67 ppm. The delays between points *a* and *b* (τ_{ab}) and points *c* and *d* (τ_{cd}) were set to 2×1.85 ms and 2×1.45 ms. This is the sequence and delays proposed by Ogura et al.[15] (e) As in (d) but optimized to give significantly better suppression levels using $\tau_{ab} = 2 \times 2.0$ ms and $\tau_{cd} = 2 \times 1.75$ ms. (f) Sequence of Figure 3a with $\tau_{ab} = 2 \times 2.2$ ms and $\tau_{cd} = 2 \times 2.0$ ms. The first WURST pulse for purging is centered at 0 ppm, covering a 60 kHz sweep range with a linear sweep rate of 2.182×10^7 Hz/s (pulse width = 2.750 ms; $B_{1,max}$ = 5 kHz), while the values for the second pulse are the same with the exception of a sweep rate of 3.347×10^7 Hz/s (pulse width = 1.793 ms; $B_{1,max}$ = 5 kHz). Note the different scales in (d) vs (e) and (f).

and have established that different secondary structures (α-helix and β-sheet) can present an arginine-rich recognition surface to the widened major groove of a distorted RNA helix.[18,42−45] NMR structural studies of the complex between N^{1-22} and *boxB* RNA will help further define the structural principles guiding protein−RNA recognition. It is clear that the quality of the resulting structure will be determined by both the number and accuracy of intermolecular contacts that can be established.

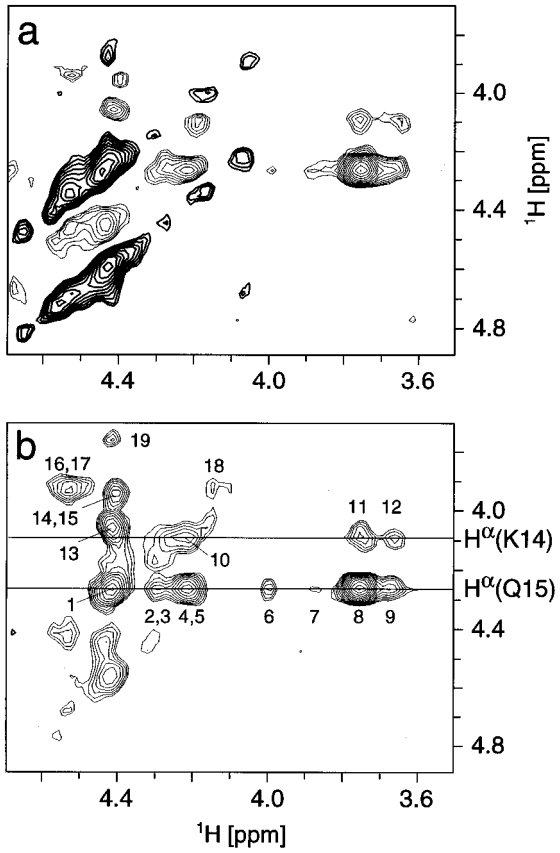

Figure 7. 2D F_1-filtered, F_2-edited NOESY spectra of unlabeled N^{1-22}/^{15}N,^{13}C labeled *boxB* RNA recorded in D_2O (τ_m = 150 ms) using the pulse schemes of Figure 3. Negative contours are indicated with darkened lines. (a) The pulse sequence described in Figure 3b was employed using parameters identical to those indicated in the legend to Figure 5a. (b) Purging experiment using the scheme of Figure 3a, a τ_a value of 1.8 ms, and a sweep rate of 2.194×10^7Hz/s (see Table 1). Crosspeaks 4, 8, and 9 are NOEs from H5′, H4′ and H5″ of adenine 9 of *boxB* RNA to the H^α of Gln 15 while cross peaks 10−12 are NOEs from H5′, H4′ and H5″ (adenine 9) to H^α of Lys 14. Note that H5′ and H5″ are not stereospecifically assigned.

An illustration of the improvement in the quality of spectra recording intermolecular NOEs obtained using filtering schemes involving WURST pulses is illustrated in Figure 7, where sections from 2D F_1-filtered, F_2-edited NOE data sets (τ_m = 150 ms) are shown. The data sets were recorded on an unlabeled N^{1-22}/^{15}N,^{13}C labeled *boxB* RNA complex in D_2O, using the sequences of Figure 3 (parts a and b). In the spectrum recorded with purging achieved using ^{13}C 90° pulses (Figure 7a) a significant residual diagonal is observed with distorted phase properties, preventing the detection of important intermolecular NOEs. In contrast, the better suppression level achieved by purging schemes using WURST pulses is evident in Figure 7b, where NOEs involving Lys14 H^α and Gln15 H^α and ribose protons of adenine 9 are clearly observed. Moreover, NOEs between nearly degenerate protons (see cross peak labeled 1 in Figure 7b) can be assigned. All of the peaks labeled in Figure 7b have been observed and assigned in a 3D ^{13}C F_1-filtered, F_3-edited NOESY-HSQC spectrum. Finally, it is noteworthy that a comparison of the intensities of cross peaks in both data sets in regions of the spectra far removed from the diagonal indicates that the increased number of ^{1}H pulses in

(42) Ye, X.; Kumar, R. A.; Patel, D. J. *Chem. Biol.* **1995**, *2*, 827.
(43) Puglisi, J. D.; Chen, L.; Blanchard, S.; Frankel, A. D. *Science* **1995**, *270*, 1200.
(44) Peterson, R. D.; Feigon, J. *J. Mol. Biol.* **1996**, *264*, 863.
(45) Ye, X.; Gorin, A.; Ellington, A. D.; Dinshaw, P. *Nature Struct. Biol.* **1996**, *3*, 1026.

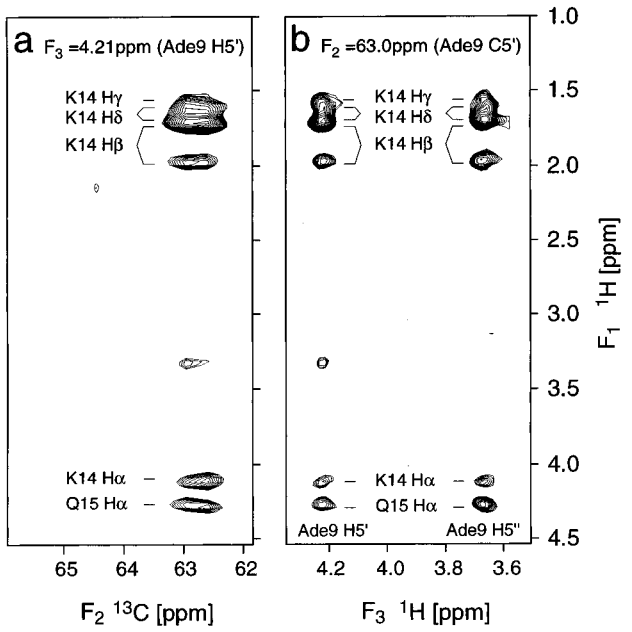

Figure 8. Selected planes from the 3D ^{13}C F_1-filtered, F_3-edited NOESY-HSQC experiment ($\tau_m = 150$ ms) of unlabeled $N^{1-22}/^{15}N,^{13}C$ labeled *boxB* RNA recorded in D_2O. Acquisition and processing parameters are given in Materials and Methods. Peptide signals are observed in F_1, while ^{13}C and ^1H chemical shifts of the RNA are recorded in F_2 and F_3, respectively. (a) ($^1H,^{13}C$) plane (F_1,F_2) at the ^1H frequency of adenine 9 H5′ (F_3 = 4.21ppm). (b) 2D (^1H, ^1H) plane (F_1,F_3) at the ^{13}C frequency of adenine 9 C5′ ($F_2 = 63.0$ ppm) showing NOE cross peaks to adenine H5′ and H5″. Note that stereospecific assignments for H5′ and H5″ have not been obtained.

the WURST-based experiment has not resulted in an attenuation of NOE intensities.

Figure 8 illustrates two cross sections from an F_1-filtered, F_3-edited data set recorded on the unlabeled $N^{1-22}/^{15}N,^{13}C$ labeled *boxB* RNA complex using the pulse sequence of Figure 3a. In Figure 8a, a ($^1H,^{13}C$) plane extracted at the ^1H chemical shift of adenine 9 H5′ (F_3) illustrates NOE contacts between H5′ of adenine 9 and protons on Lys 14 and Gln 15. The corresponding slice in Figure 8b, illustrating a portion from the ($^1H,^1H$) plane at the carbon frequency of adenine 9 C5′ shows intermolecular NOEs involving adenine 9 H5′ and H5″ to Lys 14 and Gln 15. Although Lys 14 and Gln 15 were found not to be critical for *in vivo* antitermination activity of the N protein,[46] they were proposed to be on the same face of an α-helix which interacts with the RNA. It is now clear from the present data that these residues interact with the hairpin loop of *boxB* RNA. In combination with the corresponding experiment which records intermolecular NOEs in the $^{15}N,^{13}C$ labeled N^{1-22}/unlabeled *boxB* RNA complex in H_2O (see sequence of Figure 3c) it has been possible to unambiguously assign over 75 intermolecular NOEs.

Secondary structure assignment of N^{1-22} as determined from $^1H^\alpha$, $^{13}C^\alpha$, $^{13}C^\beta$, and ^{13}CO chemical shifts using the Chemical Shift Index method[47,48] suggests the formation of an α-helix, as previously proposed on the basis of CD spectra[20] and in agreement with mutagenesis studies.[46] Although a complete description of the structure will be described elsewhere, the limited NOE information presented here agrees with previous mutational studies which suggest that one face of this α-helix interacts with *boxB* RNA.[20,46,49−52] Multiple *in vivo* and *in vitro* studies have also focused on the importance of the *boxB* RNA hairpin loop for antitermination activity and N binding,[20,46,49−52] and it is therefore not surprising to find NOE interactions to adenine 9 H5′ and H5″. Additional NOEs extracted from the improved filtered NOESY experiments presented here will be of crucial importance in the determination of the full interaction interface involving the *boxB* RNA hairpin.

Conclusion

We have described significantly improved pulse schemes for measurement of intermolecular NOEs in complexes dissolved in either D_2O or H_2O. The experiments make use of frequency swept carbon inversion pulses, which are insensitive to RF inhomogeneity. It is anticipated that the significance of these improvements will become even greater at higher magnetic field strengths where because ^{13}C rf field strengths have not kept pace with increased spectral dispersion, resonance offset effects become even more limiting. Finally, the utility of the methods is demonstrated on a peptide/RNA complex where crucial NOEs between the peptide and RNA hairpin loop that are obscured by diagonal peaks in previously published versions of the experiment are readily identified in the improved experiments.

Acknowledgment. The authors thank Mark Van Ohne (Banting and Best, Toronto) for cloning the GST-N^{1-22} construct and Joyce Li (Banting and Best, Toronto) for preparation of unlabeled and ^{13}C-labeled N^{1-22}. This research was supported by grants from the Natural Sciences and Engineering Research Council of Canada (L.E.K.) and the Medical Research Council of Canada (L.E.K and J.G.). C.Z. is the recipient of Swiss Science National Fund and Human Frontiers Science Program fellowships. S.V. is the recipient of a Swiss Science National Fund post-doctoral fellowship. P.L. is a Terry Fox Research Fellow of the National Cancer Institute of Canada supported with funds provided by the Terry Fox Run. J.G. is a distinguished scientist of the Medical Research Council of Canada and an International Research Scholar of the Howard Hughes Medical Institute. L.E.K is an Alfred P. Sloan Fellow.

JA970224Q

(46) Franklin, N. C. *J. Mol. Biol.* **1993**, *231*, 343.
(47) Wishart, D. S.; Sykes, B. D.; Richards, F. M. *Biochemistry* **1992**, *31*, 1647.
(48) Wishart, D. S.; Sykes, B. D. *Methods Enzymol.* **1994**, *239*, 363.
(49) Chattopadhyay, S.; Hung, S. C.; Stuart, A. C.; Palmer III, A. G.; Garcia-Mena, J.; Das, A.; Gottesman, M. E. *Proc. Natl. Acad. Sci. U.S.A.* **1995**, *92*, 12131.
(50) Mogridge, J.; Mah, T.-F.; Greenblatt, J. *Genes and Development* **1995**, *9*, 2831.
(51) Doelling, J. H.; Franklin, N. C. *Nucleic Acids Res.* **1989**, *17*, 5565.
(52) Cilley, C. D.; Williamson, J. R. *RNA* **1997**, *3*, 57.
(53) Bax, A.; Pochapsky, S. *J. Magn. Reson.* **1992**, *99*, 638.
(54) Marion, D.; Ikura, M.; Tschudin, R.; Bax, A. *J. Magn. Reson.* **1989**, *85*, 393.
(55) Shaka, A. J.; Barker, P. B.; Freeman, R. *J. Magn. Reson.* **1985**, *64*, 547.
(56) Shaka, A. J.; Keeler, J.; Frenkiel, T.; Freeman, R. *J. Magn. Reson.* **1983**, *52*, 335.
(57) McCoy, M. A.; Mueller, L. *J. Magn. Reson.* **1992**, *98*, 674.
(58) McCoy, M.; Mueller, L. *J. Am. Chem. Soc.* **1992**, *114*, 2108.
(59) Friedrich, J.; Davies, S.; Freeman, R. *J. Magn. Reson.* **1987**, *75*, 390.
(60) Boyd, J.; Scoffe, N. *J. Magn. Reson.* **1989**, *85*, 406.
(61) Patt, S. L. *J. Magn. Reson.* **1992**, *96*, 94.
(62) Pascal, S. M.; Muhandiram, D. R.; Yamazaki, T.; Forman-Kay, J. D.; Kay, L. E. *J. Magn. Reson. B* **1993**, *103*, 197.
(63) van de Ven, F. J. M. *Multidimensional NMR in Liquids*; VCH Publishers, Inc.: New York, 1995.